

Methods

Materials: Chitosan (CS, deacetylation: 85%), acrylamide (AAm, 99%), ammonium persulfate (APS, 96%), a polytetrafluoroethylene preparation (PTFE, 60 wt% dispersion), Lithium bis(trifluoromethanesulfonyl)imide (LiTFSI, 99.9%), and tetraethoxysilane (TEOS, 98%), Lithium manganese(III,IV) oxide (LiMn_2O_4 , 99.5%) were all purchased from J&K China Chemical Ltd and used without further purification. The activated carbon powder used (surface area of $2000 \text{ m}^2 \text{ g}^{-1}$, porous volume of 0.7 mL g^{-1}) and conductive graphite were purchased from Shenzhen BTR New Energy Materials Co., Ltd (China). The carbon cloth was purchased from Shanghai Hesun Electric Co., Ltd (China).

Preparation of PACH/SiO₂: 0.30 g AAm and 0.2g TEOS were dissolved in 2 mL CS solution (40 mg mL^{-1}), and APS (1.0 wt % of AAm) was then added into the mixture. After magnetic stirring to a clear and homogenous solution, the solution was degassed and sealed under N_2 to remove dissolved oxygen. The free-radical polymerization was processed in $50 \text{ }^\circ\text{C}$ for 12 h to form the hydrogel. Different contents (4%,8%,12%,16%) of SiO_2 were applied to determine its effect on electrolyte strength.

The as-prepared hydrogel was soaked in deionized water for 12 h to remove the unreacted monomers, and then was fully dried in an oven at $50 \text{ }^\circ\text{C}$ for 24 h. For comparison, we named the hydrogel using the same operating procedure without TEOS as PACH. And then, the freeze-dried hydrogel was soaked in LiTFSI aqueous solution (1.0 M, 2.0 M, 5.0 M, and 10.0 M) for about 24h before using (The hydrogels were

labeled as PACH/SiO₂-1, PACH/SiO₂-2, PACH/SiO₂-5 and PACH/SiO₂-10(HiSE), respectively.)

Assembly and Electrochemical Measurements of HiSE-Based EDLC & ALB: The activated carbon electrode (AC) was prepared with 80 wt% activated carbon, 10 wt% conductive graphite, and 10 wt% PTFE, and was dried in an oven at 120 °C for 1 h. The mass loading of AC electrode for the working electrode is 4.0 mg cm⁻². The assembled EDLC was a sandwich-like configuration of AC//HiSE//AC. Electrochemical performances of the EDLCs were evaluated by cyclic voltammetry (CV), galvanostatic charge-discharge (GCD), linear sweep voltammetry (LSV) and electrochemical impedance spectroscopy (EIS), which were all conducted on a CHI 660E electrochemical workstation in a two-electrode mode. CV ranged from 0 to 2.0 V with the scan rates ranged from 10 to 500 mV s⁻¹, at the same time, GCD at the current density ranged from 0.1 to 2.5 A g⁻¹. LSV tests were carried out at a scan rate of 5 mV s⁻¹ in the voltage range from 0 to 4 V. The resistance is determined by the EIS using two platinum sheets sandwiched between the hydrogel electrolytes. EIS was measured from 0.1 to 100,000 Hz with voltage amplitude of 5 mV. Ionic conductivity is calculated using the formula S7.

Similarly, LiMn₂O₄ cathode was prepared with 80 wt% LiMn₂O₄, 10 wt% conductive graphite, and 10 wt% PTFE, and was dried in an oven at 120 °C for 1 h. GCD at the current density ranged from 0.1 to 1.0 A g⁻¹. The assembled ALB was a configuration of AC//HiSE//LiMn₂O₄. The AC and LiMn₂O₄ was at weight ratio of 8:1.

Tension Experiments: The mechanical properties were measured on a commercial

tensile tester (Instron CAT.NO.: 2710-204). A piece of the original or the healed PACH/SiO₂ was cut into a strip with a size of 2.0 mm × 10 mm × 20 mm. Two ends of the sample were adhered to the plates. Then the sample was stretched at a rate of 50.0 mm min⁻¹ and its stress-strain curves were recorded.

Characterizations: SEM images were recorded by a Hitachi FE-SEM S-4800. XPS was conducted on a PHI-5700ESCA. Fourier transform infrared spectra were recorded using a Shimadzu FT-IR 8400S spectrometer. The DSC scans were conducted on a TA Instruments Q2000 scanning calorimeter at a heating rate of 5 °C min⁻¹. X-ray diffraction (XRD) patterns were collected obtained on a Bruker Smart 1000 (Bruker AXS, Inc.). The coordination states in the PACH/SiO₂ were studied via Raman spectroscopy using an NRS-5100 spectrometer (JASCO) in a laser of 532 nm. Optical images were obtained with a Canon M6 (18-150). All cycle stability and ALB data in this paper are measured using LANBTS BT-2016S.

Supplementary Note 1. self-healing properties:

Benefited from the intermolecular hydrogen bonds among the dual polymer chains, the PACH/SiO₂ possesses superior a self-healing property as Figure S3a. Two freshly cut hydrogels were contacted at room temperature. To unravel the self-healing mechanism, we applied urea to the wounds. One can find a significant decline in stress and strain after the hydrogel self-healing with the urea treatment (Figure S3b). After 60 min, the PACH/SiO₂ completely self-healed in the absence of any external stimuli and enabled to withstand extensive stretching without breaking (Figure S3c). This suggests that the observed self-healing is dominated by the formation of abundant reversible intermolecular hydrogen bonds.^{1, 2} Moreover, no deterioration was found for mechanical properties and ionic conductivity after self-healing (Figure S3e).

Supplementary Note 2. Computational Methods

Density functional theory calculations (DFT) were performed using the Becke's three parameters (B3) Exchange functional in combination with the Lee-Yang-Parr (LYP) non-local correlation functional (B3LYP) as implemented in the numeric atom-centered basis set all-electron code FHI-aims. The CS and ploy-AAm (PAAm) structures were approximated as molecules with two and three monomer units of deacetylated glucosamine and AAm, respectively. Their initial geometries ('Parent' configuration in Tables S1 and S2) were constructed using the Avogadro³ molecular editor and visualizer and pre-optimized using the universal force field as implemented in Avogadro, and then fully relaxed with FHI-aims using the Broyden-Fletcher-Goldfarb-Shanno optimization algorithm (BFGS). Those 'Parent' structures were then

used to generate *ca.* 50 different low-energy conformers pre-screened with a genetic algorithm search tool as implemented in Avogadro. And we optimized each conformer with the BFGS optimizer in FHI-aims. The energies of the gas phase optimized conformers were then calculated with an implicit solvent as implemented in FHI-aims. Also, the geometry of LiTFSI was optimized starting from already reported initial structures.⁴

The effect of the solvent was included using the recently implemented implicit solvent model based on the multipole moment expansion (MPE) method,⁵ which allows for an efficient way of including coarse salvation effects in the framework of full potential all-electron codes such as FHI-aims, where localized, atom-centered basis sets, and non-uniform integration grids are used. For the solvent, a static cavity, constructed as an iso-density surface of the initial electron density of the solute, was used with an iso-value of $0.125 \text{ e}/\text{\AA}^3$. The default parameters that control the convergence of the model, such as the expansion order of the electrostatic potential inside and outside the cavity, were sufficient to achieve good convergence. The dielectric constant (ϵ) was set to be that of water ($\epsilon = 78.35$).

The most stable CS and PAAM conformers from the MPE calculations (conf11 and conf45 in Tables S1 and S2, respectively), as well as LiTFSI, were then used to calculate their interaction with a single water molecule. Again, 56, 44, and 26 different configurations of water attached to CS, PAAM, and LiTFSI, respectively, were generated and optimized in the gas phase, and then their energies evaluated with MPE (Tables S4, S5, and S6). The interaction energies were then calculated as:

$$\Delta E_{int} = E_{MPE}([H_2O - M]) - E_{MPE}([M]) - E_{MPE}([H_2O]), \quad (S1)$$

where $M = \text{CS, PAAm, and LiTFSI}$.

We used the ‘tight’ settings, including all basis set functions up to the ‘tier2’ standard according to the FHI-aims notation. All the geometries were optimized with a residual forces threshold of 0.01 eV/\AA^{-1} ; and the convergence of the electron density, and the total energy of the system was set to 10^{-4} e , and 10^{-6} eV , respectively.

Supplementary Note 3. Flexibility and self-healing properties of Supercapacitor

Neither significant distortion occurred for the EDLC in the CV (20 mV s^{-1}) nor for GCD (2 A g^{-1}) or degradation in capacitance, even though bent to 90° or 180° and twisted 90° (Figure S10). Such excellence fully demonstrates the potential as a flexible wearable device. Nyquist impedance plots showed that a slight decrease for resistance occurred when the EDLC was bent or twisted (Figure S11b). This is due to the contact area between the electrode and electrolyte expand with bending, leading to a reduction of the interfacial resistance^{6, 7}. Yet, by using electron microscopy, no significant detachment (or peeling) was found at the electrode/electrolyte interface, neither after bending nor twisting.

The self-healing capacity of the EDLC based on HiSE was also investigated. To this end, we cut the capacitor into two halves, and then set them together for 1 h at ambient condition. In Figure S11c, the CV was almost consistent with the initial curves even after 10-cycle self-healings. Although current collectors (carbon cloth) are inherently irreparable, they can work well together after the cut/healing processes of the electrolyte. If the carbon cloth is not connected successfully after self-healing, a small

piece of carbon cloth can be used as a patch to connect the two ends.⁸ Since abundant reversible hydrogen bonds endows the hydrogel an outstanding self-healing ability, no decrease occurred in capacitance (Figure S11d).

Electrolyte uptake: The PACH/SiO₂ was fully dried in vacuum to constant weight. The dried PACH/SiO₂ samples (W_0 , g) were then immersed in LiTFSI (1M, 2M, 5M, and 10M) aqueous solution at room temperature for 12 h. The hydrogel was then removed from the LiTFSI solution, excess water on the hydrogel surface was removed using absorbent tissue paper, and the weight of the soaked PACH/SiO₂ (W_1 , g) was measured. Finally, the soaked hydrogels were dried to constant weight as PACH/SiO₂-LiTFSI (W_2 , g). The electrolyte uptake (wt %) was calculated using equation (S2-S5):

$$LiTFSI \text{ uptake (wt \%)} = \frac{W_2 - W_0}{W_0} \times 100\% \quad (S2)$$

$$y_{LiTFSI} \text{ (mmol g}^{-1}\text{)} = \frac{W_2 - W_0}{287.09 \times W_0} \quad (S3)$$

$$water \text{ uptake (wt \%)} = \frac{W_1 - W_2}{W_0} \times 100\% \quad (S4)$$

$$y_{water} \text{ (mmol g}^{-1}\text{)} = \frac{W_1 - W_2}{18 \times W_0} \quad (S5)$$

Ionic conductivity: The ionic conductivity (σ , S cm⁻¹) was calculated using equation (S6):

$$\sigma = \frac{L}{R \times A} \times 1000 \quad (S6)$$

where L (cm) is the distance between the two electrodes, A (cm²) is the effective area of the PACH/SiO₂, and R (Ω) is the bulk resistance of the PACH/SiO₂.

Electrochemical properties of the EDLC: The specific capacitance (C_{AC} , F g⁻¹) of the single AC electrode for the solid-state PACH/SiO₂-based EDLC was estimated from the GCD profiles according to the equation,

$$C_{AC} = \frac{4 \times I \times \Delta t}{m \times \Delta V} \quad (S7)$$

where m (g) is the total mass of active carbon in the two electrodes, ΔV (V) is the operating voltage on discharge (excluding the voltage drop), and Δt (s) is the time duration for a full discharge.

The energy density (E , Wh kg⁻¹) and power density (P , W kg⁻¹) of the EDLC were estimated using equations (S8) and (S9):

$$E_{EDLC} = \frac{C_{AC} \times \Delta V^2}{8} \times \frac{1000}{3600} \quad (S8)$$

$$P_{EDLC} = \frac{3600 \times E_{EDLC}}{\Delta t} \quad (S9)$$

where C_{AC} (F g⁻¹) is the specific capacitance of the single AC electrode, ΔV (V) is the voltage window on discharge (excluding the voltage drop), and Δt (s) is the time duration for a full discharge.

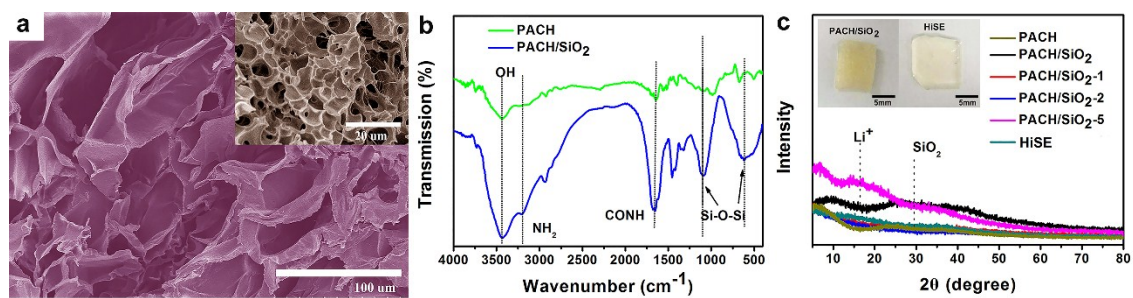


Figure S1 a) SEM for dried PACH/SiO₂ (Scale bars = 100 μm). b) FT-IR spectra. c)

XRD patterns of PACH, PACH/SiO₂, and PACH/SiO₂-x (x=1, 2, 5, 10M LiTFSI).

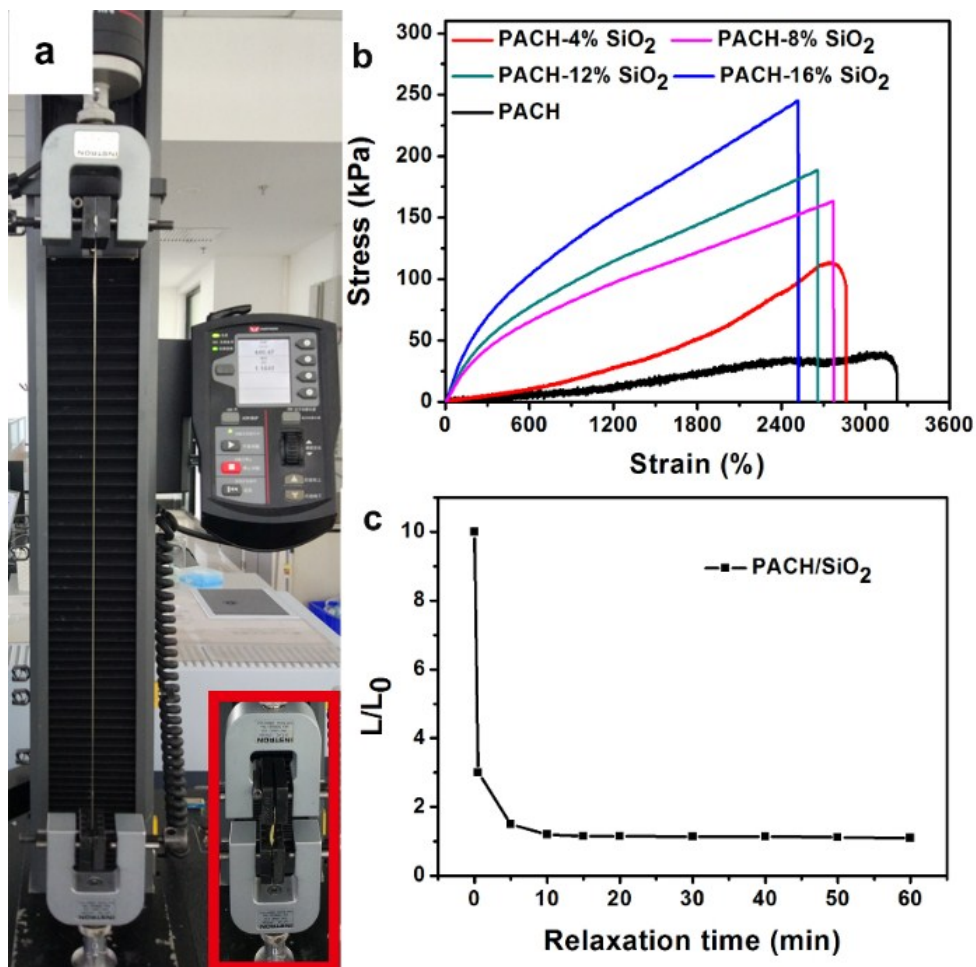


Figure S2 a) Photos illustrating the 3000% stretchability of PACH/SiO₂. b) Stress-strain curves of the PACH/SiO₂ with different concentrations of SiO₂. c) A tensile set test of original PACH/SiO₂. Stretched to ten times its original length, PACH/SiO₂ can return back to 1.1 times its original length within 60 min.

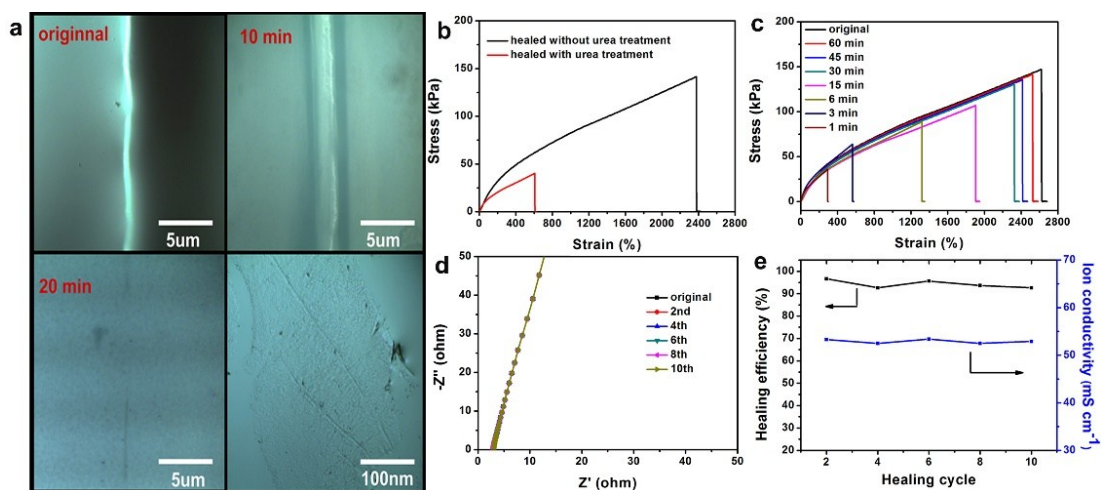


Figure S3 a) Self-healing process of PACH/SiO₂. The last picture is the observation of the repaired area enlarged to 100nm. b) Stress-strain curves of healed samples with/without urea treatment. c) Stress-strain curves of the PACH/SiO₂ for different healing time. d) Nyquist plots for PACH/SiO₂ at different concentrations of LiTFSI. e) Ionic conductivity and mechanical healing efficiency of the HiSE after multiple breaking/healing cycles.

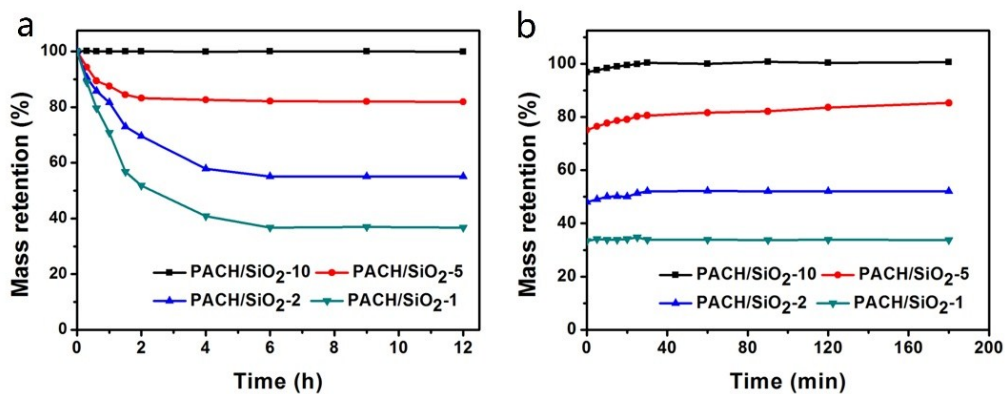


Figure S4 a) The mass of PACH/SiO₂-x in a 40% humidity atmosphere at 40 °C. b) The mass of dry PACH/SiO₂-x at different concentrations of LiTFSI in a 40% humidity atmosphere at 40 °C.

When HiSE is placed in an oven at 40 °C for 12 h, almost no mass change occurs. Whereas others lose weight (Figure S4a). Notably, dry HiSE can recover to its original weight consistently in a 40% humidity atmosphere at 40 °C within 30 min. The weight of other dry hydrogels did not change substantially, except for that PACH/SiO₂-5 slowly recovered to 85.2% after 180 min (Figure S4b). This indicates the HiSE has a strong capability to retain water and absorb water.⁹

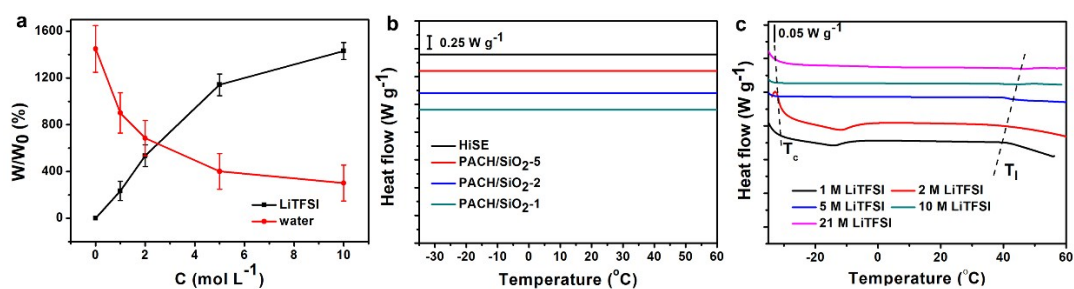


Figure S5 a) The mass concentration of water and ions inside PACH/SiO₂-x. b) DSC thermograms of PACH/SiO₂-x. c) DSC thermograms of LiTFSI at different concentration. Thermal stability was determined by crystallization (T_c) and melting (T_m) temperatures. T₁ is the initial temperature of endothermic peak.

In the LiTFSI solution, as the concentration increases, the T_c gradually decreases, and the endothermic peak gradually shifts to the right and the endothermic peak gradually decreases. This indicates that as the ion content in the solution increases, the thermal stability of the LiTFSI solution gradually increases. When the concentration is increased to 5M, a significant thermal transition disappears (1M LiTFSI for -13.9 °C and 2M LiTFSI for -11.6 °C), which is the disappearance of free water. And when the hydrogels were soaked in different concentrations of solution, there was no obvious thermal transition for all hydrogels, which proved the stability of HiSE.

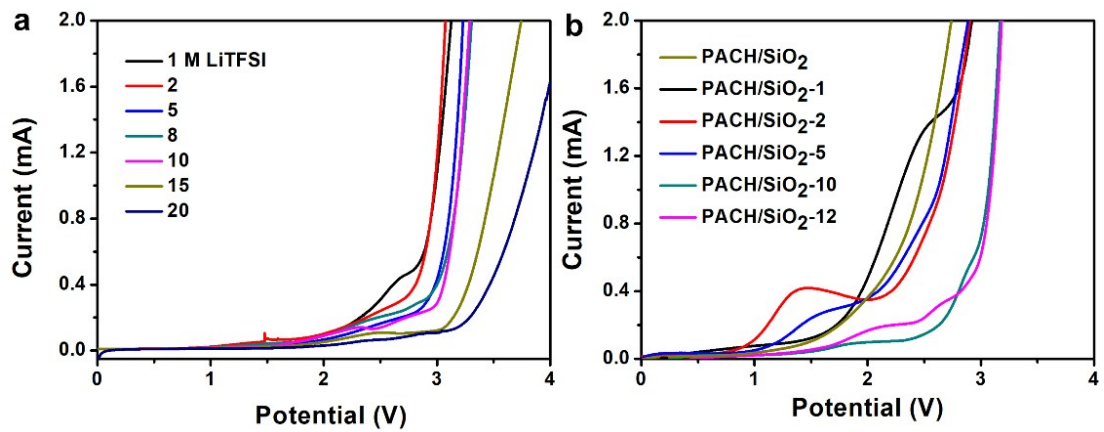


Figure S6 LSV measurement of a) WiSE and b) PACH/SiO₂-x at a scan rate of 5 mV

s⁻¹.

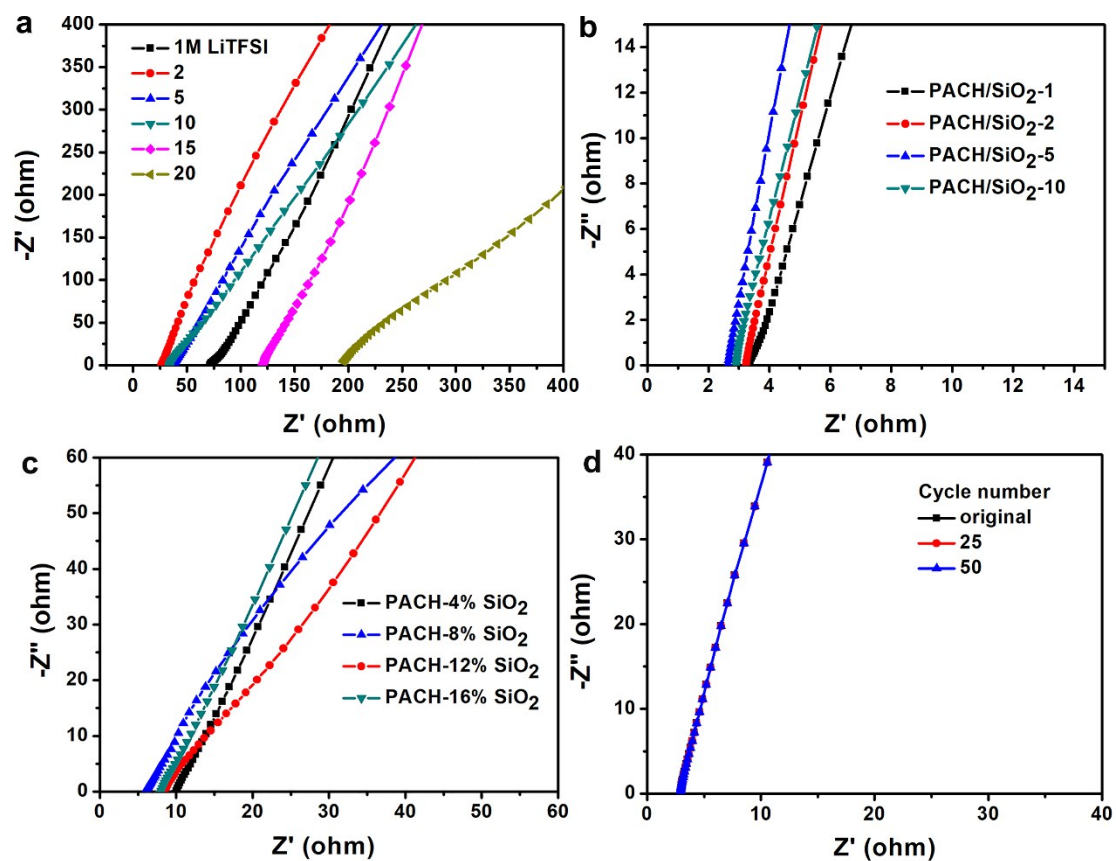


Figure S7 Nyquist plots of a) WiSE, b) PACH/SiO₂-x, c) HiSE with different concentrations of SiO₂, and d) HiSE after 50-time stretches.

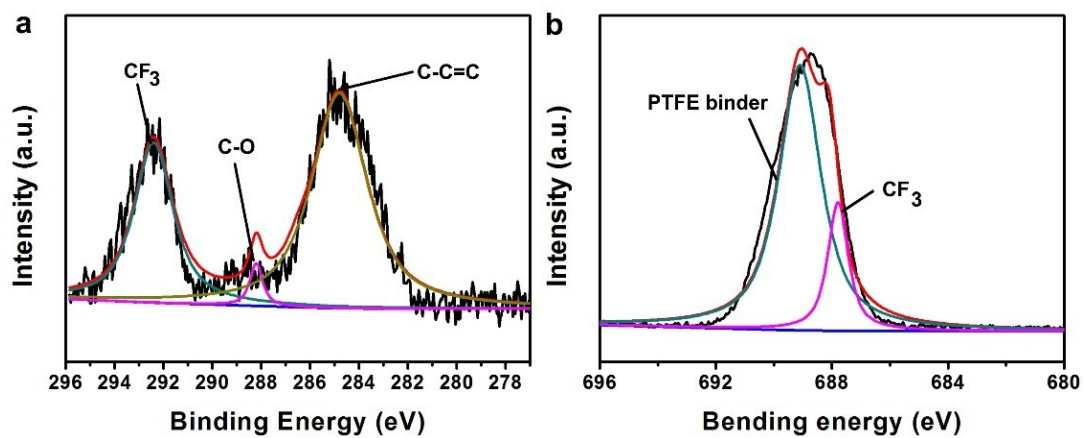


Figure S8 XPS spectra of AC electrode in HiSE for EDLC after 10 charging/discharging cycles. a) The evolution of C 1s and b) the evolution of F 1s.

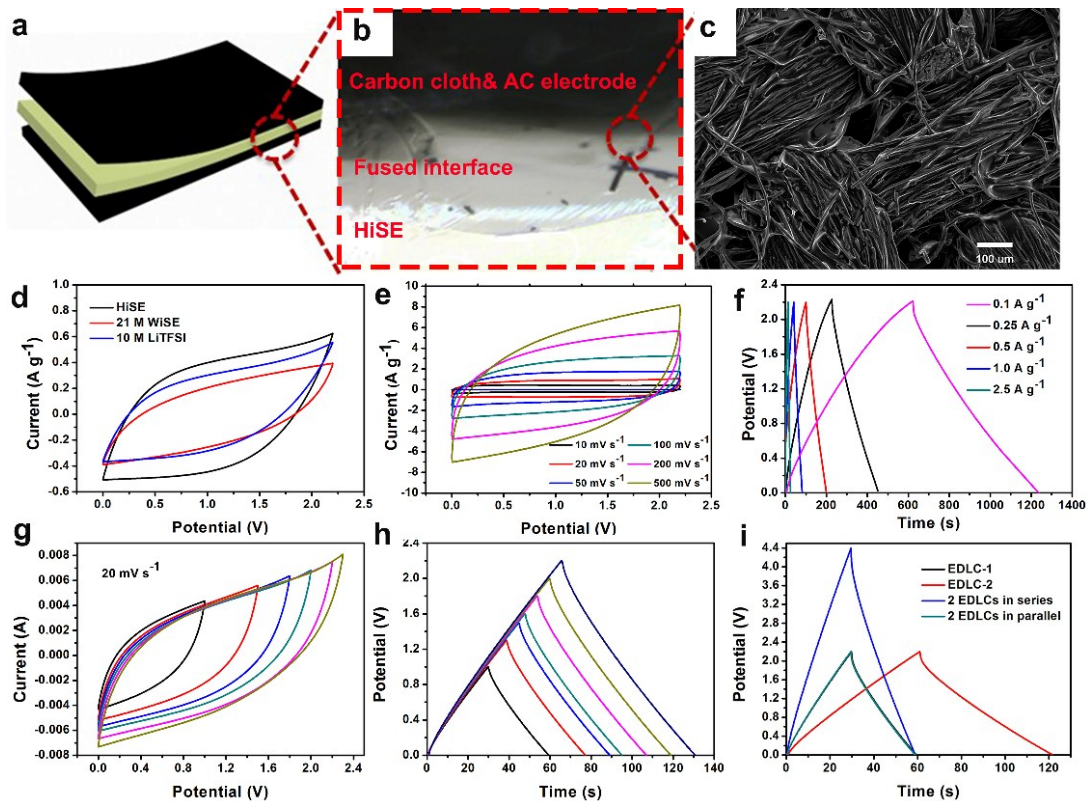


Figure S9 a) The simple sandwich structure of EDLC. b) Digital image of the electrode/electrolyte interface. c) SEM image of the carbon cloth collector. d) CV curves of in various electrolytes at a scan rate of 10 mV s^{-1} . e) CV curves and f) GCD profiles of the EDLC using WiSE. g) CV curves (20 mV s^{-1}) and h) GCD profiles (2 A g^{-1}) for different operating voltages of the EDLC using HiSE. i) GCD profiles (2 A g^{-1}) in series and in parallel.

In different operating voltages, the CV and GCD also exhibited quasirectangular and symmetrical triangular profiles, respectively. When the operating voltage exceeds 2.2 V , the capacitor is irreversible. Therefore, 2.2 V was utilized in the subsequent electrochemical tests of the EDLCs to ensure the long-term stability. Two EDLCs assembled in series yield twice the potential of a single one, whereas the connection in parallel results in twice the current density (CV) and charge-discharge time (GCD)

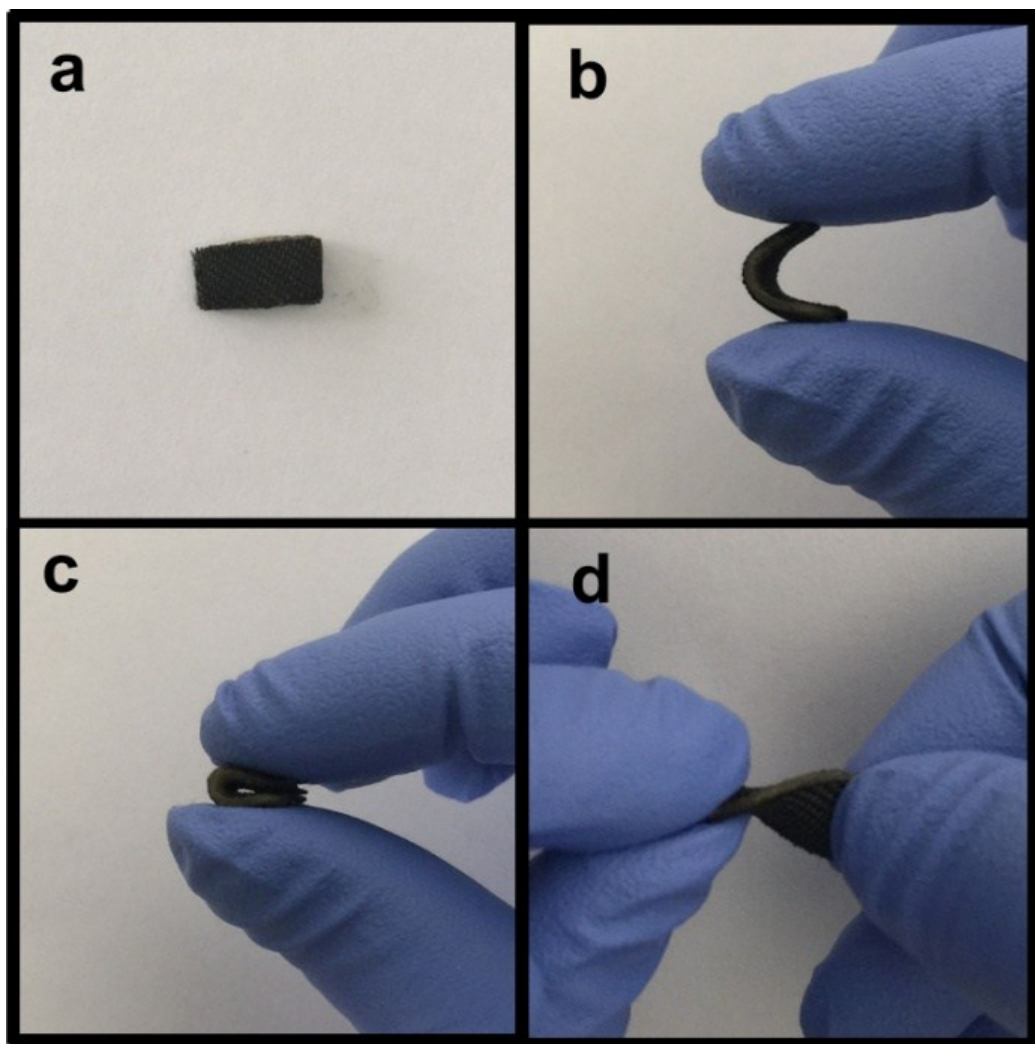


Figure S10 Digital photo of EDLC or ALB bent to 90° or 180° and twisted 90°.

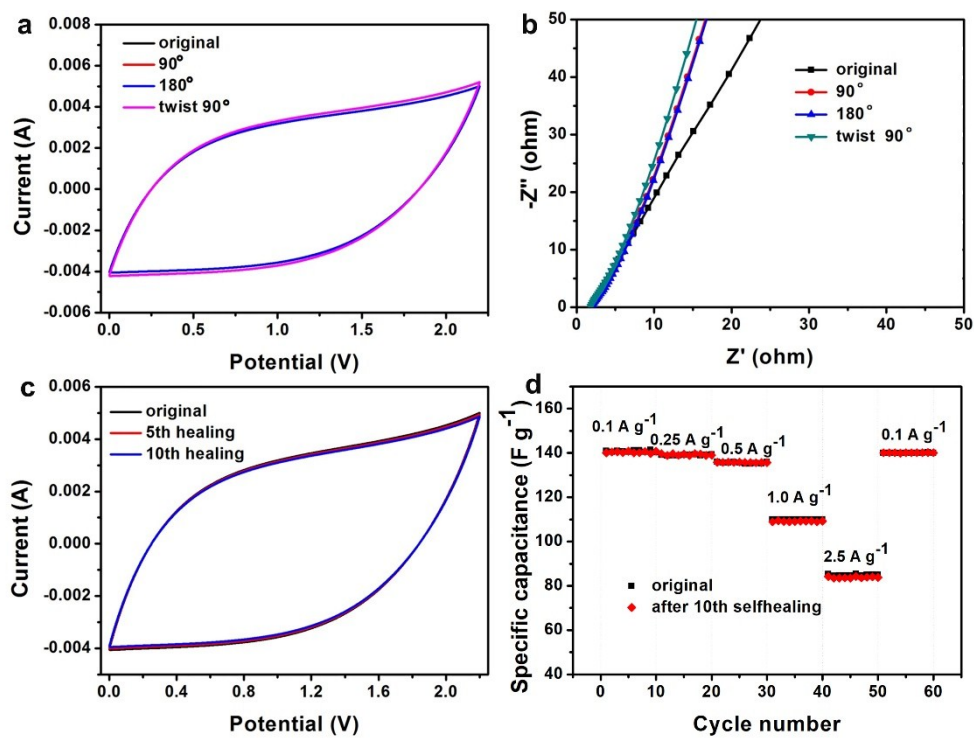


Figure S11 a) CV curves bending different angles at a scan rate of 20 mV s^{-1} . b) Nyquist plots for EDLCs bending different angles. c) CV curves for self-healing EDLCs at a scan rate of 20 mV s^{-1} . d) rate capability for self-healing EDLC.

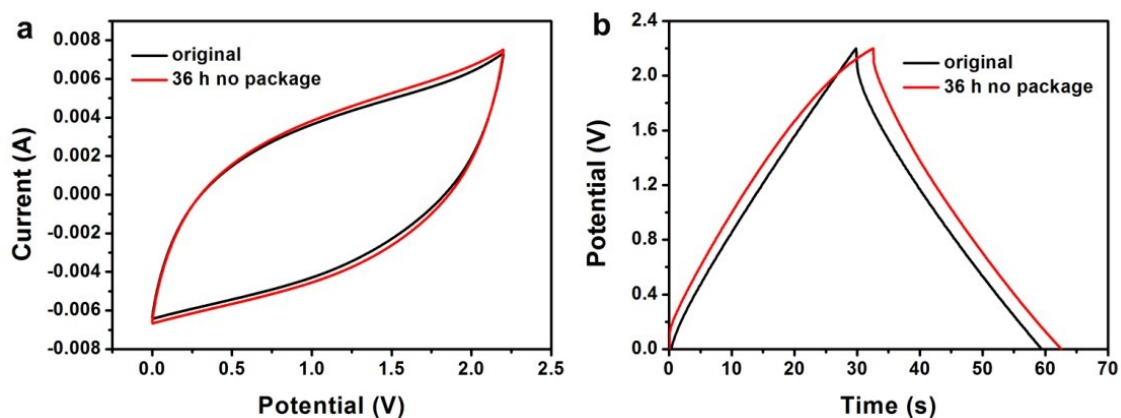


Figure S12 Electrochemical performances of EDLCs based HiSE after 36 h no package. a) CV curves for EDLCs at a scan rate of 20 mV s^{-1} . b) GCD profiles for EDLCs at a current density of 2 A g^{-1} .

The EDLC based on HiSE can keep the capacitance at the atmosphere of 40% humidity and $40 \text{ }^\circ\text{C}$ temperature for 36 h without an encapsulation. Due to the high concentration of ions inside the hydrogel, moisture is absorbed from air, which ensures the outstanding water retention of the electrolyte and the entire cell.

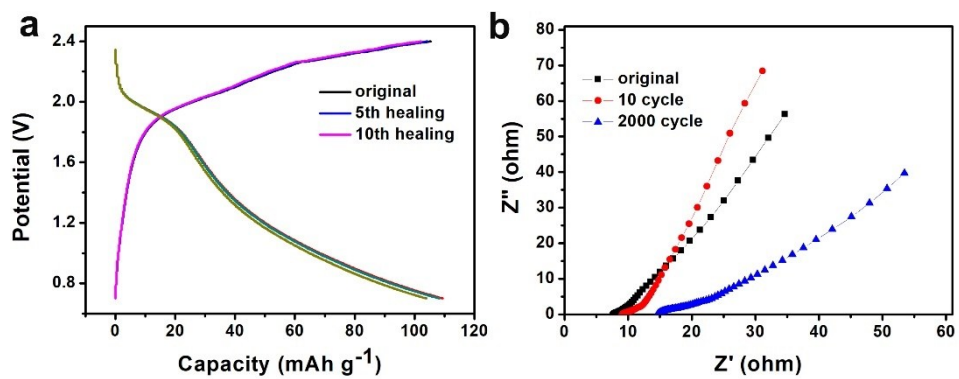


Figure S13 a) GCD profiles for self-healing ALB at a current density of 0.2 A g⁻¹. b)

Nyquist plots for ALB.

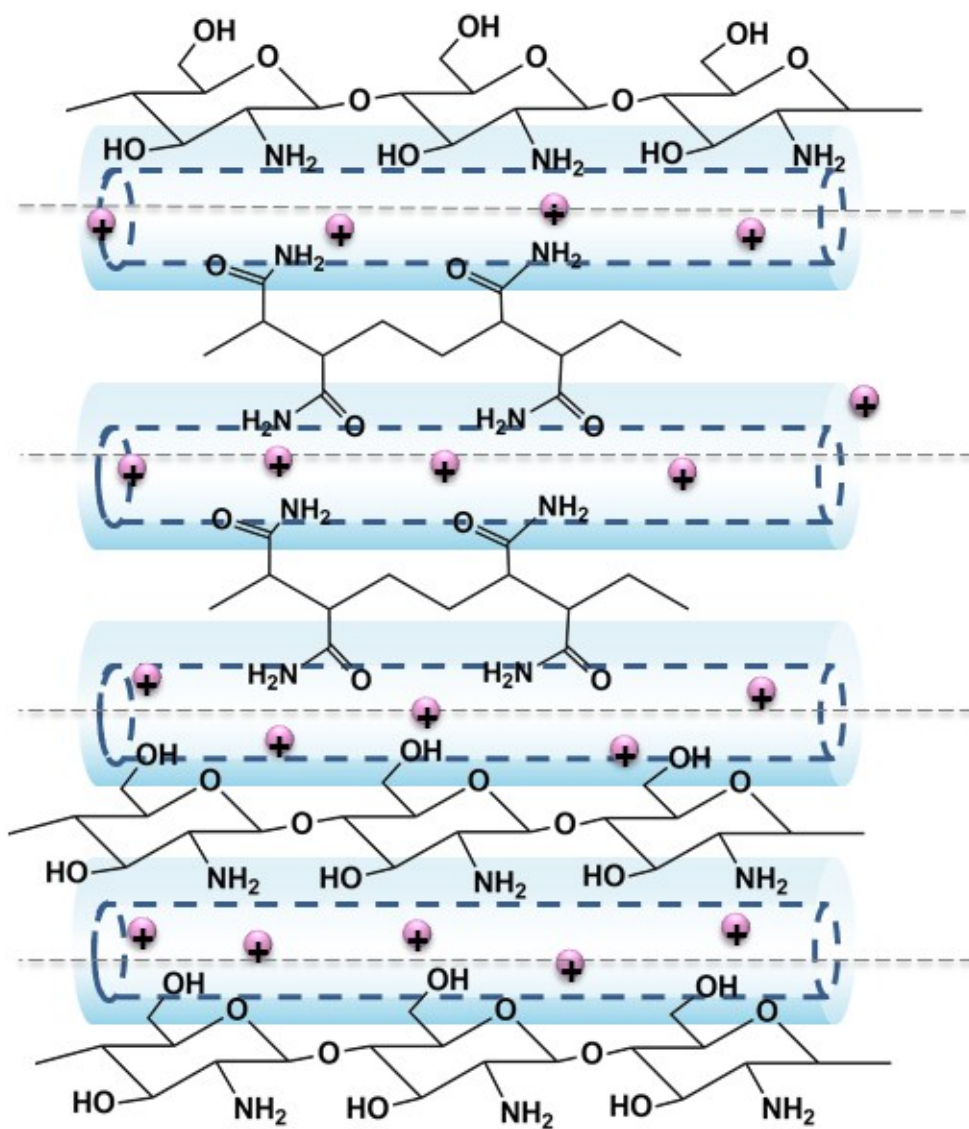


Figure S14 Simulated Li^+ channel inside HiSE.

Table S1. Computed total energies (in eV) of all investigated CS conformers considering MPE (E_{MPE}) and plain gas-phase (E_{gas}) calculations.

Conformer	E_{MPE}	E_{gas}
conf11	-34255.9830205	-34254.9686245
conf40	-34255.9684308	-34254.9913445
conf29	-34255.9664209	-34254.9779116
conf25	-34255.9443785	-34255.1854923
conf5	-34255.9390586	-34255.1322786
conf38	-34255.9226251	-34255.0295544
Parent	-34255.9195961	-34255.0325212
conf13	-34255.9168307	-34255.0323533
conf21	-34255.9160613	-34255.0363703
conf4	-34255.9152263	-34254.9952368
conf35	-34255.878186	-34254.735444
conf26	-34255.8779845	-34255.029041
conf24	-34255.8767111	-34255.0825943
conf22	-34255.8766623	-34254.9253695
conf36	-34255.876577	-34255.0912968
conf3	-34255.8732329	-34254.9373071
conf41	-34255.8606801	-34254.7333156
conf16	-34255.8591731	-34254.971949

conf39	-34255.8583809	-34254.8993396
conf19	-34255.8580223	-34255.0209894
conf43	-34255.8500804	-34254.8978477
conf49	-34255.8471147	-34254.8405031
conf46	-34255.846699	-34254.9298849
conf2	-34255.8466712	-34254.8679664
conf15	-34255.8405558	-34255.0275716
conf42	-34255.8385037	-34254.9030811
conf44	-34255.8230906	-34254.8457501
conf10	-34255.8120771	-34254.7454959
conf28	-34255.8101882	-34254.9299007
conf48	-34255.8046956	-34254.8567902
conf6	-34255.7999951	-34254.9662711
conf17	-34255.7983082	-34254.9556889
conf20	-34255.7971312	-34254.9382252
conf37	-34255.7920639	-34254.8473298
conf18	-34255.7920295	-34254.8254361
conf23	-34255.7894958	-34254.9190222
conf30	-34255.7892631	-34254.8108543
conf1	-34255.7850747	-34254.7841334
conf32	-34255.7615755	-34254.861568
conf31	-34255.7564337	-34254.8515794

conf33	-34255.753464	-34254.6801501
conf14	-34255.7517129	-34254.9645979
conf9	-34255.7297129	-34254.8929789
conf27	-34255.7209495	-34254.7211832
conf7	-34255.6998856	-34254.8694516
conf8	-34255.6734788	-34254.6271491
conf45	-34255.6537543	-34254.5527119
conf47	-34255.6400218	-34254.6757674
conf50	-34255.6135945	-34254.7758079
conf12	-34255.6080874	-34254.7205008
conf34	-34255.5242261	-34254.6998878

Table S2. Computed total energies (in eV) of all investigated PAAm conformers considering MPE (E_{MPE}) and plain gas-phase (E_{gas}) calculations.

Conformer	E_{MPE}	E_{gas}
conf45	-21305.4979384	-21304.7319008
conf1	-21305.4595617	-21304.7166116
conf23	-21305.4276383	-21304.6202147
conf26	-21305.4093699	-21304.5615815
conf21	-21305.4048887	-21304.65699
conf34	-21305.3902589	-21304.4184735
conf27	-21305.3658618	-21304.4251426
conf28	-21305.3598841	-21304.4496467
conf38	-21305.354683	-21304.4787807
conf2	-21305.3471531	-21304.4488943
conf3	-21305.3442854	-21304.4932297
conf36	-21305.3311744	-21304.4170003
conf35	-21305.331101	-21304.5796757
conf18	-21305.3294879	-21304.2870494
conf12	-21305.3119085	-21304.3858207
conf20	-21305.3106796	-21304.5397834
conf19	-21305.3060911	-21304.2959634
conf16	-21305.3051655	-21304.4018022

conf7	-21305.303076	-21304.2685754
conf9	-21305.3022029	-21304.1998487
conf15	-21305.298352	-21304.3117804
conf6	-21305.2961696	-21304.459856
conf8	-21305.2955467	-21304.3677403
conf33	-21305.2907549	-21304.493509
conf4	-21305.2861363	-21304.3318061
conf46	-21305.2796724	-21304.2579922
conf24	-21305.2783736	-21304.3473189
conf41	-21305.2757804	-21304.3126209
conf48	-21305.2623494	-21304.3440306
conf39	-21305.2594522	-21304.2531062
conf44	-21305.2574244	-21304.5067251
conf22	-21305.239592	-21304.2809019
conf11	-21305.2377007	-21304.3008749
conf17	-21305.2354103	-21304.2378536
conf25	-21305.2233219	-21304.2095035
conf37	-21305.222882	-21304.0971707
conf32	-21305.2196257	-21304.4249473
conf13	-21305.2180464	-21304.0674765
conf40	-21305.2127554	-21304.3516173
conf42	-21305.2086205	-21304.4426444

conf30	-21305.2015883	-21304.3213269
conf10	-21305.1832747	-21304.1234996
Parent	-21305.166284	-21304.4430531
conf47	-21305.1649773	-21304.4429347
conf29	-21305.1495394	-21304.3418711
conf31	-21305.1205163	-21304.2279938
conf43	-21305.1063765	-21304.2371494
conf14	-21305.099853	-21304.289986
conf5	-21305.0377159	-21304.2682944

Table S3. Computed total energies (in eV) of H₂O and LiTFSI species considering MPE (E_{MPE}) and plain gas-phase (E_{gas}) calculations.

Species	E_{MPE}	E_{gas}
H ₂ O	-2081.20912622	-2080.956316562
LiTFSI	-49947.099612352	-49945.961109802

Table S4. Computed total energies (in eV) of all investigated CS conformers including one explicit water molecule and considering MPE (E_{MPE}) and plain gas-phase (E_{gas}) calculations.

Conformer	E_{MPE}	E_{gas}
conf2	-36337.6463115	-36336.8388683
conf52	-36337.6392755	-36336.8385347
conf45	-36337.5397124	-36336.4471047
conf9	-36337.5035569	-36336.5477318
conf40	-36337.4469908	-36336.4405843
conf32	-36337.4403066	-36336.3666511
conf48	-36337.4394599	-36336.3663988
conf23	-36337.4394322	-36336.3665016
conf26	-36337.4392554	-36336.3667336
conf10	-36337.4391948	-36336.4413453
conf7	-36337.4389126	-36336.366449
conf6	-36337.4384534	-36336.3656852
conf56	-36337.4372887	-36336.3660265
conf34	-36337.4353931	-36336.3439089
conf15	-36337.4347374	-36336.4417587
conf37	-36337.4330922	-36336.4257149
conf3	-36337.4317655	-36336.4263399
conf54	-36337.4315943	-36336.4267474

conf33	-36337.4285809	-36336.4262618
conf38	-36337.4205063	-36336.4334979
conf50	-36337.4199007	-36336.4335494
conf16	-36337.4188669	-36336.4343549
conf20	-36337.4185431	-36336.4345197
conf1	-36337.4095901	-36336.3307953
conf31	-36337.4004748	-36336.2674244
conf51	-36337.3980338	-36336.2680803
conf29	-36337.3977962	-36336.2678302
conf39	-36337.3921193	-36336.2781132
conf24	-36337.3921052	-36336.2669661
conf12	-36337.390887	-36336.3219544
conf11	-36337.3776138	-36336.2731906
conf17	-36337.3748628	-36336.287387
conf4	-36337.3741221	-36336.2760598
conf43	-36337.3651655	-36336.3346225
conf8	-36337.3634684	-36336.333757
conf5	-36337.3611908	-36336.3199769
conf19	-36337.3605057	-36336.3197567
conf46	-36337.3552522	-36336.2746795
conf21	-36337.3412863	-36336.2886914
conf18	-36337.3393814	-36336.2207627

conf53	-36337.3372569	-36336.2880418
conf27	-36337.3368413	-36336.2876951
conf55	-36337.3358868	-36336.2881421
conf28	-36337.3353611	-36336.2880098
conf44	-36337.33285	-36336.2050511
conf30	-36337.3318886	-36336.2055493
conf35	-36337.331085	-36336.2873378
conf25	-36337.3063456	-36336.2026135
conf49	-36337.2868943	-36336.2799211
conf47	-36337.2858266	-36336.2816218
conf41	-36337.2778549	-36336.2634955
conf42	-36337.2757314	-36336.263158
conf14	-36337.2748673	-36336.262929
conf13	-36337.2737328	-36336.2631066
conf36	-36337.2647321	-36336.1711078

Table S5. Computed total energies (in eV) of all investigated PAAm conformers including one explicit water molecule and considering MPE (E_{MPE}) and plain gas-phase (E_{gas}) calculations.

Conformer	E_{MPE}	E_{gas}
conf25	-23387.0535969	-23386.2145137
conf10	-23386.9034453	-23386.0761952
conf24	-23386.9003746	-23386.075949
conf4	-23386.8902302	-23386.0578198
conf38	-23386.887457	-23386.0580354
conf33	-23386.8794889	-23386.0518256
conf26	-23386.8782213	-23386.1233097
conf32	-23386.8780947	-23386.0518656
conf37	-23386.8768648	-23386.0611498
conf17	-23386.876363	-23386.0969906
conf18	-23386.876363	-23386.0969906
conf43	-23386.8761022	-23386.0514151
conf5	-23386.8759107	-23386.0971306
conf35	-23386.875661	-23386.0965626
conf15	-23386.8747073	-23386.0971621
conf34	-23386.8738628	-23386.0968888
conf16	-23386.873826	-23386.1187071
conf27	-23386.8730628	-23386.0968799

conf9	-23386.87176	-23386.0964915
conf36	-23386.8572619	-23386.0720713
conf2	-23386.85689	-23386.072006
conf8	-23386.845679	-23386.1042567
conf11	-23386.8453105	-23386.1041267
conf6	-23386.8450672	-23386.1040001
conf14	-23386.8427382	-23386.1035754
conf28	-23386.8358491	-23386.1034201
conf42	-23386.8349234	-23386.1033076
conf3	-23386.8341957	-23386.1034429
conf12	-23386.824709	-23386.0607715
conf31	-23386.8235285	-23386.0608526
conf41	-23386.823215	-23386.0610173
conf30	-23386.8231253	-23386.0609256
conf13	-23386.8209955	-23385.9545801
conf44	-23386.820276	-23385.9542999
conf39	-23386.8194105	-23385.863105
conf7	-23386.8186353	-23385.9539048
conf1	-23386.818413	-23385.9539919
conf40	-23386.8176313	-23385.9541193
conf21	-23386.8159383	-23385.9871069
conf29	-23386.8145691	-23385.9870644

conf23	-23386.8107297	-23385.9524244
conf20	-23386.809774	-23385.8927836
conf19	-23386.7779337	-23385.8646171

Table S6. Computed total energies (in eV) of all investigated LiTFSI conformers including one explicit water molecule and considering MPE (E_{MPE}) and plain gas-phase (E_{gas}) calculations.

Conformer	E_{MPE}	E_{gas}
conf2	-52028.4710218	-52027.7160016
conf21	-52028.4694991	-52027.7159132
conf20	-52028.4687906	-52027.7156936
conf5	-52028.4227488	-52027.0999446
conf3	-52028.3917636	-52027.0855571
conf1	-52028.3910978	-52027.1184053
conf12	-52028.3907914	-52027.1184807
conf6	-52028.3889503	-52027.1184748
conf24	-52028.3882851	-52027.0856831
conf9	-52028.3646824	-52027.1161583
conf7	-52028.3638513	-52027.1156339
conf11	-52028.3621574	-52027.7803429
conf16	-52028.3618108	-52027.7810062
conf8	-52028.3616648	-52027.1159713
conf13	-52028.3614114	-52027.7807627
conf26	-52028.3613491	-52027.780188
conf10	-52028.3612104	-52027.7807287
conf15	-52028.3610753	-52027.7807646

conf14	-52028.361015	-52027.7808649
conf22	-52028.3599847	-52027.779729
conf4	-52028.3592771	-52027.7805387
conf18	-52028.3585429	-52027.779844
conf17	-52028.358244	-52027.7798816
conf23	-52028.3574325	-52027.7793491
conf19	-52028.3538034	-52027.779187
conf25	-52028.3019005	-52026.9863647

Table S7. Properties of conventional WiSE.

Electrolyte	Conductivity (mS cm ⁻¹)	Voltage (V)	Na ⁺ (Li ⁺)/water molar ratio	Electrolyte state
21 M LiTFSI ¹⁰	~10	3.0	0.38:1	liquid
5 M LiTFSI/CH ₃ CN ¹¹	6.8	3.0	0.38:1	liquid
32 m KOAc–8 m LiOAc ¹²	5.3	3.0	0.79:1	liquid
Li(TFSI) _{0.7} (BETI) _{0.3} · 2H ₂ O ¹³	3.0	3.0	0.5:1	liquid
17 M NaClO ₄ ¹⁴	-	2.7	0.31:1	liquid
HiSE (This work)	51.3	2.6	0.33:1	hydrogel

Table S8. Properties of conventional hydrogel electrolyte.

Electrolyte	Electrode	Voltage (V)	Specific capacitance (F g ⁻¹)	Energy density (W h kg ⁻¹)
HiSE (This work)	AC	2.2	140.1	23.54
PVAPB ¹⁵	AC	2.0	91.8	9.2
PVA-Na ₂ SO ₄ ¹⁶	AC	1.8	124	13
PVA-[BMIM]Cl ¹⁷	FCNT-Coated Cellulose Paper	1.6	188	16.3

PVAPB represents PVA potassium borate; [BMIM]Cl represents 1-butyl-3-methylimidazolium chloride; FCNT represent functionalized carbon nanotube.

References

1. D. L. Taylor and M. In Het Panhuis, *Adv. Mater.*, 2016, **28**, 9060-9093.
2. P. Cordier, F. Tournilhac, C. Soulie-Ziakovic and L. Leibler, *Nature*, 2008, **451**, 977-980.
3. M. D. Hanwell, D. E. Curtis, D. C. Lonie, T. Vandermeersch, E. Zurek and G. R. Hutchison, *Journal of Cheminformatics*, 2012, **4**, 17-34.
4. H. Zhang, O. Arcelus and J. Carrasco, *Electrochim. Acta*, 2018, **280**, 290-299.
5. M. Sinstein, C. Scheurer, S. Matera, V. Blum, K. Reuter and H. Oberhofer, *Journal of Chemical Theory and Computation*, 2017, **13**, 5582-5603.
6. Y. Huang, M. Zhong, F. K. Shi, X. Y. Liu, Z. J. Tang, Y. K. Wang, Y. Huang, H. Q. Hou, X. M. Xie and C. Y. Zhi, *Angew. Chem. Int. Ed.*, 2017, **56**, 9141-9145.
7. M. Zhong, X. Y. Liu, F. K. Shi, L. Q. Zhang, X. P. Wang, A. G. Cheetham, H. Cui and X. M. Xie, *Soft matter*, 2015, **11**, 4235-4241.
8. Y. Huang, M. Zhong, Y. Huang, M. Zhu, Z. Pei, Z. Wang, Q. Xue, X. Xie and C. Zhi, *Nat. Commun.*, 2015, **6**, 10310.
9. X. Peng, H. Liu, Q. Yin, J. Wu, P. Chen, G. Zhang, G. Liu, C. Wu and Y. Xie, *Nat. Commun.*, 2016, **7**, 11782.
10. L. M. Suo, O. Borodin, T. Gao, M. Olguin, J. Ho, X. L. Fan, C. Luo, C. S. Wang and K. Xu, *Science*, 2015, **350**, 938-943.
11. Q. Dou, S. Lei, D.-W. Wang, Q. Zhang, D. Xiao, H. Guo, A. Wang, H. Yang, Y. Li, S. Shi and X. Yan, *Energy Environ. Sci.*, 2018, **11**, 3212-3219.
12. M. R. Lukatskaya, J. I. Feldblyum, D. G. Mackanic, F. Lissel, D. L. Michels, Y. Cui and Z. Bao, *Energy Environ. Sci.*, 2018, **11**, 2876-2883.
13. Y. Yamada, K. Usui, K. Sodeyama, S. Ko, Y. Tateyama and A. Yamada, *Nat. Energy*, 2016, **1**, 16129-16138.
14. M. H. Lee, S. J. Kim, D. Chang, J. Kim, S. Moon, K. Oh, K.-Y. Park, W. M. Seong, H. Park, G. Kwon, B. Lee and K. Kang, *Mater. Today*, 2019, DOI: 10.1016/j.mattod.2019.02.004.
15. M. Jiang, J. Zhu, C. Chen, Y. Lu, E. S. Pampal, L. Luo, P. Zhu and X. Zhang, *J. Mater. Chem. A*, 2016, **4**, 16588-16596.
16. N. Batische and E. Raymundo-Piñero, *J. Power Sour.*, 2017, **348**, 168-174.
17. X. H. Tang, Y. H. Lui, A. R. Merhi, B. L. Chen, S. W. Ding, B. W. Zhang and S. Hu, *ACS Appl. Mater. Interfaces*, 2017, **9**, 44429-44440.